

Direct Design of Closed-loop Demodulators for Amplitude Modulation Atomic Force Microscopy

Michael G. Ruppert¹, David M. Harcombe¹, Steven I. Moore¹ and Andrew J. Fleming¹

Abstract—A fundamental component of the z-axis feedback loop in amplitude modulation atomic force microscopy is the demodulator. It dictates both bandwidth and noise in the amplitude and phase estimate of the cantilever deflection signal. In this paper, we derive a linear time-invariant model of a closed-loop demodulator with user definable tracking bandwidth and sensitivity to other frequency components. A direct demodulator design method is proposed based on the reformulation of the Lyapunov filter as a modulated-demodulated controller in closed loop with a unity plant. Simulation and experimental results for a higher order Lyapunov filter as well as Butterworth and Chebyshev type demodulators are presented.

I. INTRODUCTION

Since atomic force microscopy (AFM) was invented in the late 1980s [1], the instrument has become a key enabling technology for object and material property analysis at the nanoscale [2]. Dynamic imaging modes and particularly amplitude-modulation AFM are preferred for the investigation of delicate matter and biological samples due to the low tip-sample forces [3]. This operating mode makes use of the direct excitation of the cantilever at one of its resonance frequencies and consequently requires a demodulator to obtain amplitude and phase of the cantilever deflection signal.

As a component of the z-axis feedback loop, the tracking bandwidth and sensitivity to other frequency components of the demodulator are especially important in high-speed [4] and multifrequency AFM [5] applications. As the tracking bandwidth directly affects the achievable scan rate, it should be maximized; however, this also increases the noise bandwidth. On the other hand, in multifrequency AFM applications [6]–[8], the sensitivity to other frequency components is of greatest concern.

A number of demodulation techniques can be found in the existing literature, where only a few have found regular use in commercial AFM systems [9]. For instance, RMS-to-DC conversion has low implementation complexity but is sensitive to other frequency components. In contrast, the lock-in amplifier [10] is a narrowband technique that is insensitive to other frequencies but has a limited bandwidth. Due to the simplicity and tunable performance, this method has become the standard in commercial AFM systems.

For high-speed AFM applications such as for the study of fast biological processes [11], fast single wave detectors like the peak hold method [12], coherent demodulator [13], time-varying Kalman filter [14] and Lyapunov filter [15]

have been developed. The two latter methods are closed-loop demodulators based on a linear parametric model of the cantilever deflection signal and can be extended to estimate multiple frequencies for multifrequency AFM [16], [17]. While these system based filters achieve the highest tracking bandwidth without distortion, their first order response provides limited rejection of broadband noise and other frequency components near the carrier frequency [9].

This paper presents a linear time invariant (LTI) model of the time-varying Lyapunov filter which enables the direct design of a closed loop demodulator with arbitrary transfer function. A higher order Lyapunov filter, Butterworth and Chebyshev type 1 demodulator are presented in simulation and experiment which achieve a significant improvement in sensitivity to other frequency components which is a critical performance criteria in multifrequency AFM.

II. LINEAR TIME-VARYING DEMODULATOR MODEL

A. Sinusoidal Model

Consider a sine wave with carrier frequency f_c , time-varying amplitude $A(t)$, and phase $\phi(t)$ of the form

$$u(t) = A(t) \sin(\omega_c t + \phi(t)). \quad (1)$$

The model can be linearly parametrized by applying trigonometric identities, so that the state vector $\mathbf{x} = [x_1 \ x_2]^T$ represents the quadrature and in-phase components (time-dependencies are dropped for ease of readability).

$$\begin{aligned} u(t) &= [\cos(\omega_c t) \ \sin(\omega_c t)] [A \sin(\phi) \ A \cos(\phi)]^T \\ &= \mathbf{c}(t)\mathbf{x}. \end{aligned} \quad (2)$$

Once the signal (1) is parametrized according to (2), the amplitude and phase can be recovered by

$$A = \sqrt{x_1^2 + x_2^2}, \quad \phi = \arctan\left(\frac{x_1}{x_2}\right). \quad (3)$$

B. Linear Time-varying Lyapunov Filter

The Lyapunov filter is a time-varying online adaptive estimator based on the linear parametrization of the signal (1) with exponential convergence properties [18]. The estimator can be written in the compact form [15]

$$\begin{aligned} \dot{\mathbf{x}} &= \gamma \mathbf{c}(t)^T W(s)(u - y) \\ y &= \mathbf{c}(t)\mathbf{x} \end{aligned} \quad (4)$$

where $W(s)$ is a LTI transfer function, γ is the gain parameter for tuning the bandwidth and y is the estimate of the input signal u . If $W(s)$ is chosen to be strictly positive real, a Lyapunov stability proof can be used to show the

¹School of Electrical Engineering and Computing, The University of Newcastle, Callaghan, NSW, 2308, Australia.
 Michael.Ruppert@newcastle.edu.au, David.Harcombe@uon.edu.au,
 Steven.I.Moore@uon.edu.au, Andrew.Fleming@newcastle.edu.au.

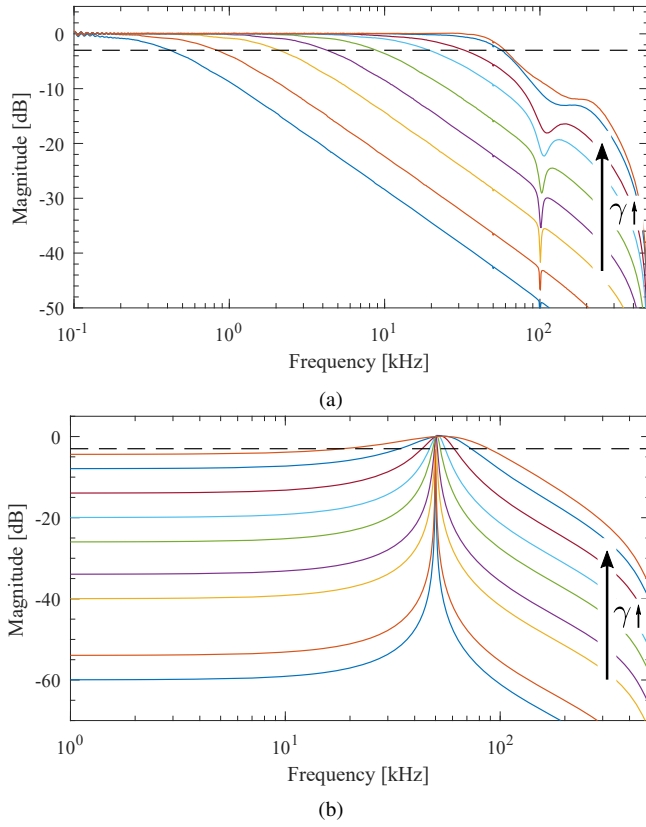


Fig. 1. (a) Simulated amplitude tracking frequency response and (b) simulated off-mode rejection of (4) for increasing γ values.

boundedness of the estimation error [18]. If $W(s) = 1$, the Lyapunov filter achieves maximum tracking bandwidth [15] but is sensitive to other frequencies due to its equivalent first order response [9]. Amplitude and phase are recovered by employing the output equations (3).

C. Simulation: Tracking Bandwidth

The tracking bandwidth is evaluated by simulating the system (4) with an input signal (1) with modulated amplitude $A(t) = 1 + \sin(2\pi f_m(t)t)$ where $f_m(t)$ is the modulation frequency which is swept for varying γ -values. The obtained frequency responses are shown in Fig. 1(a). Since the modulation frequency is varied, the output of the estimator is also modulated at f_m and the amplitude value is extracted using a numerical lock-in amplifier. The simulation uses a modeled carrier frequency of $f_c = 50$ kHz and sampling frequency $f_s = 1$ MHz. The maximum achievable tracking bandwidth, measured as the -3 dB point is approximately f_c .

D. Simulation: Sensitivity to other Frequencies

The sensitivity to other frequencies, termed off-mode rejection, is evaluated by simulating the system (4) with an input signal (1) where $A = 1$ and $f_c(t)$ is swept for varying γ -values. The obtained frequency responses are shown in Fig. 1(b). Since a fixed carrier frequency is modeled in (4), the output of the estimator is at DC. This value is extracted by calculating the value of the FFT of the amplitude estimate at zero frequency using a second-order Goertzel algorithm [19].

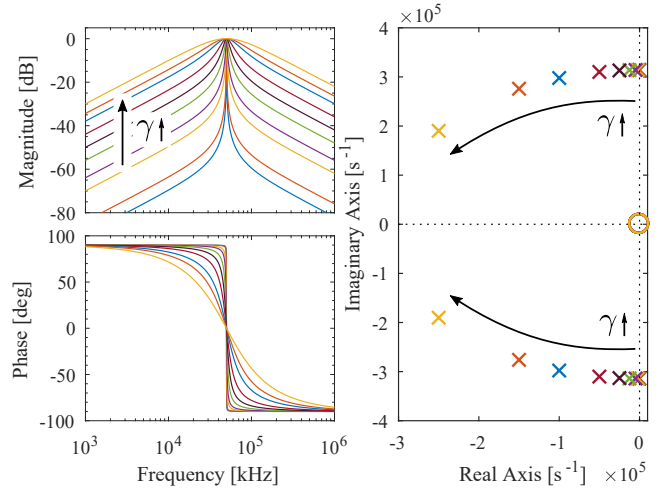


Fig. 2. Frequency response and pole-zero map of (9) from $u \rightarrow y$ for increasing γ values as indicated by the arrows.

The difference between the magnitude at unmodeled and at the modeled frequency (0 dB) is defined off-mode rejection which indicates the amount of suppression of unmodeled frequency components.

III. LINEAR TIME-INVARIANT DEMODULATOR MODEL

A. Linear Time-invariant Lyapunov Filter

Assuming $W(s) = 1$, (4) can be rewritten as

$$\begin{aligned} \dot{\mathbf{x}} &= \mathbf{M}(t)\mathbf{x} + \gamma \mathbf{c}^T(t)u \\ y &= \mathbf{c}(t)\mathbf{x} \end{aligned} \quad (5)$$

with

$$\mathbf{M}(t) = \begin{bmatrix} -\gamma \cos \theta^2 & -\gamma \sin \theta \cos \theta \\ -\gamma \sin \theta \cos \theta & -\gamma \sin^2 \theta \end{bmatrix} \quad (6)$$

where $\theta = \omega_c t$ and $\mathbf{M}(t)$ is the time-varying system matrix. A LTI formulation can be obtained by applying a coordinate transformation with a time-varying transformation matrix $\mathbf{T}(t)$ [14] such that

$$\tilde{\mathbf{x}} = \mathbf{T}(t)\mathbf{x} \iff \mathbf{x} = \mathbf{T}^{-1}(t)\tilde{\mathbf{x}} \quad (7)$$

where

$$\mathbf{T}(t) = \begin{bmatrix} \cos \theta & \sin \theta \\ -\omega \sin \theta & -\omega \cos \theta \end{bmatrix}. \quad (8)$$

The LTI system can be obtained by calculating

$$\begin{aligned} \dot{\tilde{\mathbf{x}}} &= \dot{\mathbf{T}}(t)\mathbf{x} + \mathbf{T}(t) = \begin{bmatrix} -\gamma & 1 \\ -\omega_c^2 & 0 \end{bmatrix} \tilde{\mathbf{x}} + \begin{bmatrix} \gamma \\ 0 \end{bmatrix} u \\ y &= \mathbf{c}(t)\mathbf{T}^{-1}(t)\tilde{\mathbf{x}} = \begin{bmatrix} 1 & 0 \end{bmatrix} \tilde{\mathbf{x}}. \end{aligned} \quad (9)$$

The transfer function from $u \rightarrow y$ of the system is a resonant bandpass filter of the form

$$\tilde{G}(s) = \frac{\gamma s}{s^2 + \gamma s + \omega_c^2}. \quad (10)$$

The pole-zero map and Bode plot of (9) from $u \rightarrow y$ for varying γ values is shown in Fig. 2. It can be seen that the system has a zero at the origin and a complex conjugate

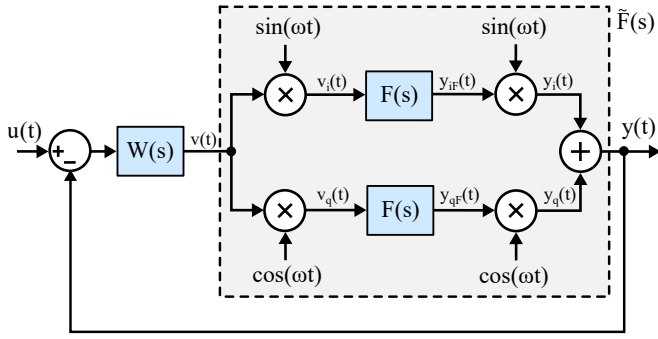


Fig. 3. Block diagram of the general closed-loop demodulator structure.

pole pair. As γ is increased, the poles move along a circle with radius ω_c further into the left half plane, representing a faster system with increased damping; critical damping is achieved at $\gamma = 2\omega_c$. The frequency responses roll off on either side of the modeled carrier frequency due to the zero at the origin and relative degree of 1. The Bode plot shows the system response ($u \rightarrow y$) in contrast to the simulated off-mode rejection $u \rightarrow A$ shown in Fig. 1(b).

B. General LTI Demodulator Model

In order to obtain an arbitrary demodulator response, consider the generalized block diagram and signal definitions in Fig. 3, where the integrator of the Lyapunov filter is replaced by the transfer function $F(s)$. In this form, the general demodulator resembles a modulated-demodulated control loop [20] with a pre-filter $W(s)$ and a unity plant.

The Laplace transform of the input signal $v(t)$ mixed with in-phase and quadrature sinusoids is

$$V_i(s) = \mathcal{L}\{v(t) \sin(\omega t)\} = \frac{1}{2j}[V(s - j\omega) - V(s + j\omega)]$$

$$V_q(s) = \mathcal{L}\{v(t) \cos(\omega t)\} = \frac{1}{2}[V(s - j\omega) + V(s + j\omega)]. \quad (11)$$

Similarly, the in-phase and quadrature outputs after mixing are

$$Y_i(s) = \mathcal{L}\{\sin(\omega t)y_{iF}(t)\}$$

$$= -\frac{1}{2}[F(s - j\omega)[V(s - 2j\omega) - V(s)] - F(s + j\omega)[V(s) - V(s + 2j\omega)]] \quad (12)$$

and

$$Y_q(s) = \mathcal{L}\{\cos(\omega t)y_{qF}(t)\}$$

$$= \frac{1}{2}[F(s - j\omega)[V(s - 2j\omega) + V(s)] + F(s + j\omega)[V(s) + V(s + 2j\omega)]]. \quad (13)$$

By summing the two branches, the nonlinear products are canceled out and the equivalent demodulator filter $\tilde{F}(s)$ can be written as

$$\tilde{F}(s) = \frac{1}{2}(F(s - j\omega) + F(s + j\omega)) \quad (14)$$

and the overall input-output transfer function is

$$\tilde{G}(s) = \frac{Y(s)}{U(s)} = \frac{W(s)\tilde{F}(s)}{1 + W(s)\tilde{F}(s)}. \quad (15)$$

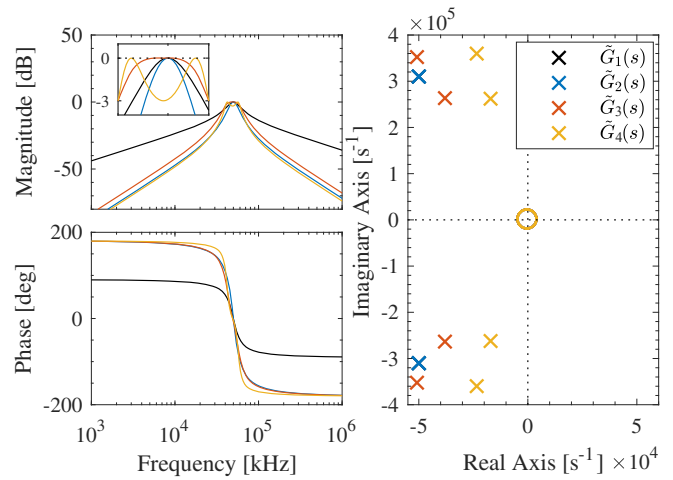


Fig. 4. Comparison of closed loop demodulator transfer functions: Lyapunov filter $\tilde{G}_1(s)$, higher order Lyapunov filter $\tilde{G}_2(s)$, Butterworth filter $\tilde{G}_3(s)$ and Chebyshev Type 1 filter $\tilde{G}_4(s)$.

Assuming $W(s) = 1$, the demodulator design problem is to find $F(s)$ from $\tilde{F}(s)$ given a desired closed loop transfer function $\tilde{G}(s)$. However, $\tilde{F}(s)$ must be representable by a complex conjugate filter pair. A parametrization with real-valued coefficients only exists for a limited number of $\tilde{G}(s)$ prototypes such as for the standard Lyapunov filter (10). Rather than solving the desired closed-loop response for $F(s)$, an alternative is to fix $\tilde{F}(s)$ and use pole-placement to find $W(s)$ such that the desired closed-loop poles are obtained.

IV. CLOSED-LOOP DEMODULATOR EXAMPLES

This section demonstrates how higher order closed-loop demodulators can be derived using standard controller design methods. The four different desired demodulator transfer functions are: the Lyapunov filter $\tilde{G}_1(s)$, higher order Lyapunov filter $\tilde{G}_2(s)$, Butterworth filter $\tilde{G}_3(s)$ and Chebyshev Type 1 filter $\tilde{G}_4(s)$ and are shown in Fig. 4.

A. Higher Order Lyapunov Filter

In order to increase the off-mode rejection, the order of the equivalent overall transfer function can be increased, for example, by combining two standard Lyapunov filters in series

$$\tilde{G}_2(s) = \frac{(\gamma s)^2}{(s^2 + \gamma s + \omega_c^2)^2}. \quad (16)$$

The design problem is cast as a standard pole placement controller design with one degree of freedom. Assuming $F_2(s) = \gamma/s$ leads to

$$\tilde{F}_2(s) = \frac{\gamma s}{s^2 + \omega_c^2}. \quad (17)$$

Solving (15) for $W(s)$ yields

$$W(s) = \frac{\tilde{G}_2(s)}{(1 - \tilde{G}_2(s))\tilde{F}_2(s)} = \frac{\gamma s}{s^2 + 2\gamma s + \omega_c^2}. \quad (18)$$

The bode plot and pole-zero map of these transfer functions for a fixed $\gamma = 200k$ resulting in a tracking bandwidth of

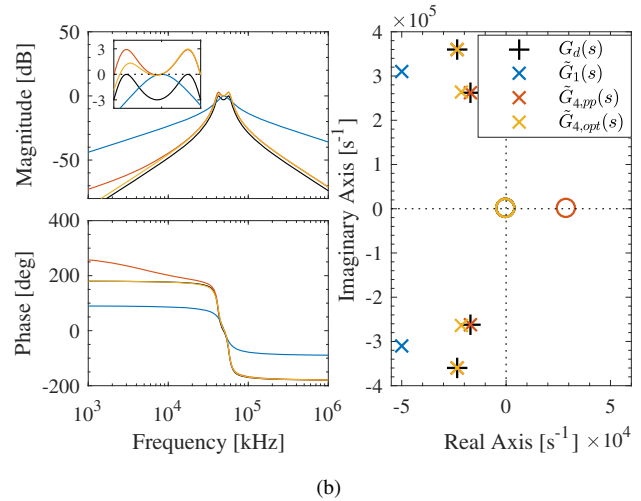
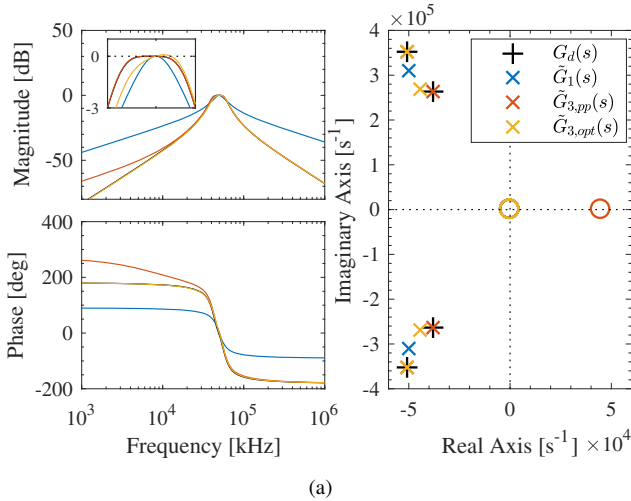


Fig. 5. Direct design of (a) second-order Butterworth demodulator and (b) Chebyshev type 1 demodulator with a tracking bandwidth of 10 kHz using exact pole placement and an approximation using pole placement optimization.

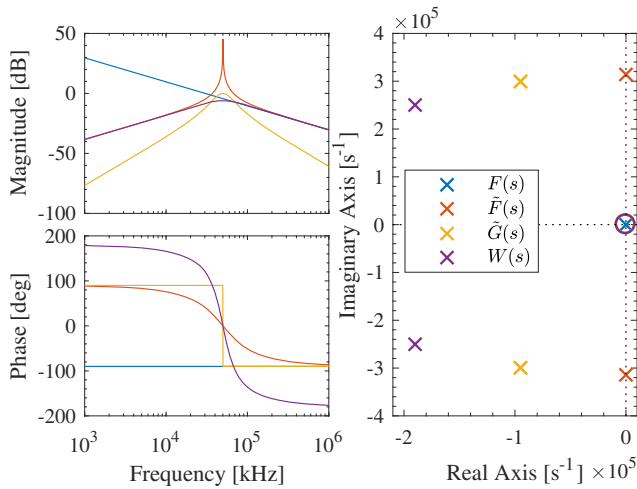


Fig. 6. Bode and pole zero plot of the higher order Lyapunov filter $\tilde{G}_2(s)$ for a fixed $\gamma = 200k$ resulting in a tracking bandwidth of 10 kHz.

10 kHz is shown in Fig. 6. The overall transfer function $\tilde{G}_2(s)$ has a double zero at the origin and a double complex conjugate pole pair at the frequency to be demodulated. This results in a steeper roll-off on either side of the carrier frequency, resulting in higher off-mode rejection. An increase in tracking bandwidth is achieved by increasing γ in both $F(s)$ and $W(s)$.

B. Butterworth and Chebyshev Filters

The desired closed-loop responses are Butterworth and Chebyshev Type 1 bandpass filters with 40 dB/dec roll-off. These filters have the form

$$G_d(s) = \frac{B_d(s)}{A_d(s)} = \frac{b_2 s^2}{s^4 + a_3 s^3 + a_2 s^2 + a_1 s + a_0} \quad (19)$$

where b_2, a_i are the filter coefficients which can be calculated based on the order and the desired tracking bandwidth ω_n

around the carrier frequency $\omega_c \pm \omega_n$. Similar to the higher order Lyapunov filter, these filters have a double zero at the origin and two complex conjugate pole pairs. The locations of the poles result in maximum flatness around the carrier frequency for the Butterworth filter or define the allowable passband ripple (here 3 dB) for the Chebyshev filter.

Having defined a desired closed loop polynomial with the five coefficients, direct pole placement can be used to calculate the filter coefficients of the prototype

$$W(s) = \frac{p_1 s + p_0}{l_2 s^2 + l_1 s + l_0} \quad (20)$$

by solving the pole-assignment equation

$$A_d(s) = L(s)A_d(s) + P(s)B_d(s). \quad (21)$$

The resulting closed loop demodulators $\tilde{G}_{3,pp}$ and $\tilde{G}_{4,pp}$ with a tracking bandwidth of 10 kHz are shown in Fig. 5(a) and (b) respectively. In both cases, it can be seen that the poles are placed accurately, yielding a well-defined frequency response around the carrier, however a non-minimum phase zero is introduced which degrades off-mode rejection performance at low frequencies. If this is unacceptable, then the double zero at the origin can be forced into $\tilde{F}(s)$, reducing the number of coefficients in $W(s)$. Non-linear pole-placement optimization can be used to place the poles as close as possible to the desired poles, which degrades performance around the carrier frequency but improves the low-frequency off-mode rejection. The resulting closed loop demodulators $\tilde{G}_{3,opt}$ and $\tilde{G}_{4,opt}$ are shown in Fig. 5. The higher order Lyapunov filter can be regarded as a special case of filters of the form (19) for which the complex poles coincide leading to a double zero at the origin and well defined response around the carrier frequency.

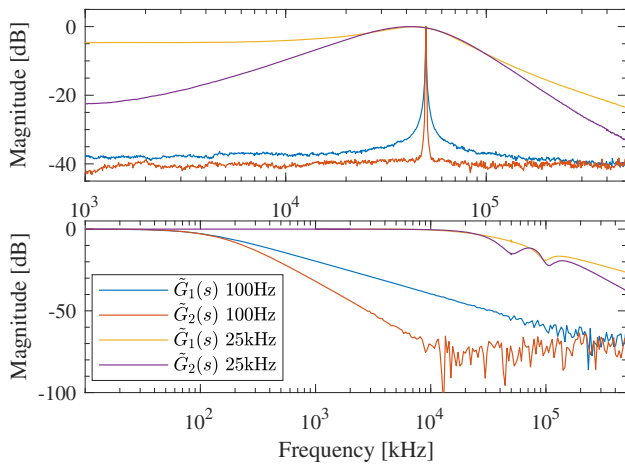


Fig. 7. Experimental off-mode rejection $u \rightarrow \hat{A}$ and tracking bandwidth frequency response of the standard and higher order Lyapunov filter.

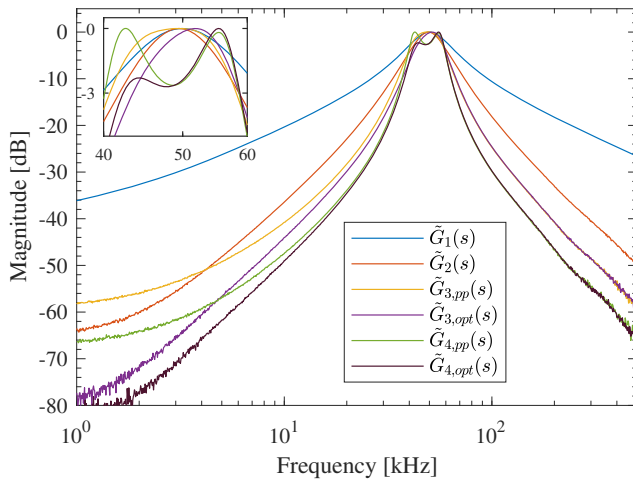


Fig. 8. Experimental off-mode frequency response of the standard Lyapunov filter \tilde{G}_1 , higher order Lyapunov filter \tilde{G}_2 , Butterworth \tilde{G}_3 and Chebyshev Demodulator \tilde{G}_4 .

V. EXPERIMENTAL RESULTS

A. Frequency Responses

The closed-loop demodulators were implemented with a fixed tracking bandwidth of 10 kHz on a Field Programmable Gate Array (FPGA) (Xilinx Kintex-7 KC705 evaluation board). The off-mode frequency responses from $u \rightarrow y$ and the off-mode rejection $u \rightarrow \hat{A}$ were measured by performing a frequency sweep on the carrier frequency (Zurich instruments HF2LI). The tracking bandwidth is half the width around the bandpass peak where the magnitude drops below -3 dB.

The two Lyapunov filters corresponding to $\tilde{G}_1(s)$ and $\tilde{G}_2(s)$ are directly compared in Fig. 7 for two bandwidth settings of 100 Hz and 25 kHz. For both the low and high bandwidth setting, the off-mode rejection is improved due to the steeper roll-off of the filter around the carrier frequency.

The off-mode frequency responses from $u \rightarrow y$ of all

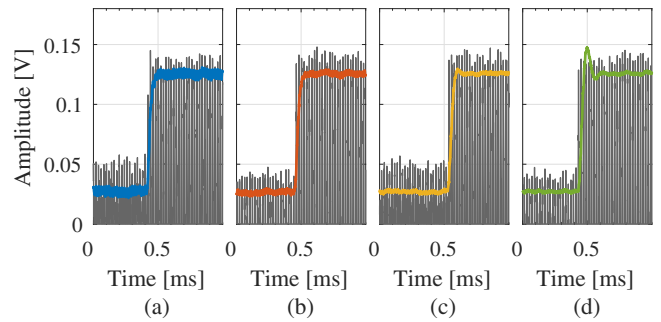


Fig. 9. Time-domain tracking experiment with (a) standard Lyapunov filter \tilde{G}_1 , (b) higher order Lyapunov filter \tilde{G}_2 , (c) Butterworth $\tilde{G}_{3,pp}$ and (d) Chebyshev Demodulator $\tilde{G}_{4,pp}$. Color-coded according to Fig. 8.

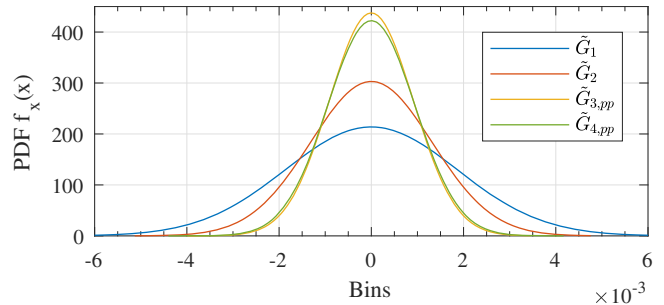


Fig. 10. Probability density function (PDF) fit to the histograms obtained from the amplitude estimates shown in in Fig. 9, color-coded accordingly.

implemented demodulators are plotted in Fig. 8. It can be observed that the desired responses are obtained around the carrier frequency. While the direct pole placement design for the Butterworth $\tilde{G}_{3,pp}$ and Chebyshev Type 1 demodulator $\tilde{G}_{4,pp}$ yields a well-defined response around the carrier frequency, the non-minimum phase zero causes the responses to flatten out for lower frequencies. This effect is mitigated by employing pole placement optimization to obtain $\tilde{G}_{3,opt}$ and $\tilde{G}_{4,opt}$. As predicted by simulation, the Chebyshev Type 1 demodulator achieves the steepest roll-off and therefore the highest off-mode rejection near the carrier frequency.

B. Time-domain Tracking

A time-domain experiment was conducted to investigate the noise present within the amplitude estimates of the demodulators and is shown in Fig. 9. The input signal to the demodulators is a square-modulated sine-wave with a second harmonic component and 2.2 MHz bandwidth limited additive white noise $y = A_1(t) \sin(\omega_c t) + A_2(t) \sin(2\omega_c t) + v$ where $A_1 = 500$ mV_{pp}, $v = 100$ mV_{pp} and $A_2 = 50$ mV_{pp}. The second harmonic component is a common artifact during tapping-mode AFM imaging. To compare the amount of noise in the amplitude estimate, a probability density function (PDF) fit to the area normalized histograms obtained from the amplitude estimate is shown in Fig. 10.

The results show that the lower order Lyapunov filter passes more additive white noise and second harmonic distortion into the amplitude estimate. At equal tracking bandwidths, the higher order Lyapunov filter, Butterworth

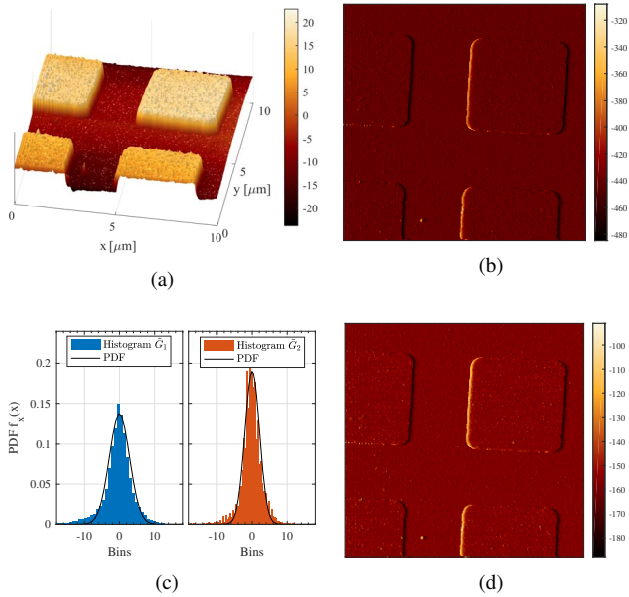


Fig. 11. (a) Topography image [nm], second harmonic magnitude image [mV] using (b) the standard Lyapunov filter \tilde{G}_1 and (d) the higher order Lyapunov filter. (c) Magnitude histogram and PDF function fit of the higher harmonic images.

filter and Chebyshev type 1 demodulator have less noise in the amplitude estimate due to the higher off-mode rejection. The Chebyshev type demodulator shows the characteristic overshoot in the time-domain response.

C. AFM Higher Harmonic Imaging

In order to demonstrate the effect of increased demodulator off-mode rejection, tapping-mode AFM imaging is performed with additional imaging on the second higher harmonic. The higher harmonic magnitude image is generated with the standard Lyapunov filter and subsequently with the higher order Lyapunov filter at an equal tracking bandwidth of 10 kHz. The HS-20MG calibration standard was imaged at 5.21 Hz over an area of $10 \mu\text{m} \times 10 \mu\text{m}$.

The AFM images are shown in Fig. 11. In the higher harmonic magnitude images, contrast is observed at the edges of the features of the sample. It can be noticed that the higher harmonic image generated by the higher order Lyapunov filter in Fig. 11(d) shows qualitatively better contrast than the standard Lyapunov filter in Fig. 11(b). This can be quantified by plotting the magnitude histogram in Fig. 11(c) for which the higher order Lyapunov filter shows a smaller standard deviation. This is due to the higher off-mode rejection which reduces the noise in the amplitude estimate of the second harmonic.

VI. CONCLUSION

In this work, LTI models are described for the off-mode rejection and tracking bandwidth of a time-varying Lyapunov filter. These models serve as a basis to directly design demodulators with arbitrary closed-loop transfer functions. This approach is demonstrated by designing demodulators

with arbitrary responses including a higher order bandpass response, Butterworth response, and Chebyshev type 1 response. The higher order responses provide improved off-mode rejection, which was experimentally verified by time-domain, frequency-domain and AFM experiments.

REFERENCES

- [1] G. Binnig, C. F. Quate, and C. Gerber, "Atomic force microscope," *Phys. Rev. Lett.*, vol. 56, pp. 930–933, March 1986.
- [2] Y. Martin, C. Williams, and H. Wickramasinghe, "Atomic force microscope-force mapping and profiling on a sub 100-Å scale," *J. Appl. Phys.*, vol. 61, no. 10, pp. 4723–4729, 1987.
- [3] R. García and R. Perez, "Dynamic atomic force microscopy methods," *Surface Science Reports*, vol. 47, no. 6–8, pp. 197 – 301, 2002.
- [4] N. Kodera, D. Yamamoto, R. Ishikawa, and T. Ando, "Video imaging of walking myosin v by high-speed atomic force microscopy," *Nature*, vol. 468, no. 7320, pp. 72–76, 2010.
- [5] R. García and E. T. Herruzo, "The emergence of multifrequency force microscopy," *Nature Nanotechnology*, vol. 7, pp. 217–226, 2012.
- [6] S. D. Solares, S. An, and C. J. Long, "Multi-frequency tapping-mode atomic force microscopy beyond three eigenmodes in ambient air," *Beilstein Journal of Nanotechnology*, vol. 5, pp. 1637–1648, 2014.
- [7] A. Raman, S. Trigueros, A. Cartagena, A. P. Z. Stevenson, M. Susilo, E. Nauman, and S. Antoranz Contera, "Mapping nanomechanical properties of live cells using multi-harmonic atomic force microscopy," *Nature Nanotechnology*, vol. 6, no. 12, pp. 809–814, 2011.
- [8] D. Forchheimer, R. Forchheimer, and D. B. Haviland, "Improving image contrast and material discrimination with nonlinear response in bimodal atomic force microscopy," *Nature communications*, vol. 6, no. 6270, pp. 1–5, 2015.
- [9] M. G. Ruppert, D. M. Harcombe, M. R. P. Ragazzon, S. O. R. Moheimani, and A. J. Fleming, "A review of demodulation techniques for dynamic mode atomic force microscopy," *Beilstein Journal of Nanotechnology*, 2017, under review.
- [10] C. R. Cosens, "A balance-detector for alternating-current bridges," *Proceedings of the Physical Society*, vol. 46, no. 6, p. 818, 1934.
- [11] T. Ando, T. Uchihashi, and T. Fukuma, "High-speed atomic force microscopy for nano-visualization of dynamic biomolecular processes," *Progress in Surface Science*, vol. 83, no. 7–9, pp. 337–437, 2008.
- [12] T. Ando, N. Kodera, E. Takai, D. Maruyama, K. Saito, and A. Toda, "A high-speed atomic force microscope for studying biological macromolecules," *Proceedings of the National Academy of Sciences*, vol. 98, no. 22, pp. 12468–12472, 2001.
- [13] D. Y. Abramovitch, "Coherent demodulation with reduced latency adapted for use in scanning probe microscopes," US Patent 20100128342, May, 2010.
- [14] M. G. Ruppert, K. S. Karvinen, S. L. Wiggins, and S. O. Reza Moheimani, "A Kalman filter for amplitude estimation in high-speed dynamic mode atomic force microscopy," *IEEE Trans. Contr. Syst. Technol.*, vol. 24, no. 1, pp. 276–284, January 2016.
- [15] M. R. P. Ragazzon, M. G. Ruppert, D. M. Harcombe, A. J. Fleming, and J. T. Gravdahl, "Lyapunov estimator for high-speed demodulation in dynamic mode atomic force microscopy," *IEEE Transactions on Control Systems Technology*, vol. 26, no. 2, pp. 765–772, 2017.
- [16] M. G. Ruppert, D. M. Harcombe, and S. O. R. Moheimani, "High-bandwidth demodulation in MF-AFM: A Kalman filtering approach," *IEEE/ASME Trans. Mechatron.*, vol. 21, no. 6, pp. 2705–2715, Dec 2016.
- [17] D. M. Harcombe, M. G. Ruppert, M. R. P. Ragazzon, and A. J. Fleming, "Lyapunov estimation for high-speed demodulation in multifrequency atomic force microscopy," *Beilstein Journal of Nanotechnology*, vol. 9, pp. 490–498, 2018.
- [18] P. A. Ioannou and J. Sun, *Robust adaptive control*. Mineola, New York: Dover Publications, Inc., 2012.
- [19] J. G. Proakis and D. G. Manolakis, *Digital Signal Processing: Principles, Algorithms, and Applications*, 3rd ed. Upper Saddle River, NJ: Prentice Hall, 1996.
- [20] K. S. Karvinen and S. O. R. Moheimani, "Modulated-demodulated control: Q control of an AFM microcantilever," *Mechatronics*, vol. 24, no. 6, pp. 661 – 671, 2014.